



MIT Open Access Articles

Global drainage patterns and the origins of topographic relief on Earth, Mars, and Titan

The MIT Faculty has made this article openly available. **Please share** how this access benefits you. Your story matters.

Citation	Black, Benjamin A., et al. "Global Drainage Patterns and the Origins of Topographic Relief on Earth, Mars, and Titan." <i>Science</i> , vol. 356, no. 6339, May 2017, pp. 727–31.
As Published	http://dx.doi.org/10.1126/SCIENCE.AAG0171
Publisher	American Association for the Advancement of Science (AAAS)
Version	Author's final manuscript
Citable link	http://hdl.handle.net/1721.1/118324
Terms of Use	Article is made available in accordance with the publisher's policy and may be subject to US copyright law. Please refer to the publisher's site for terms of use.

1 Global drainage patterns and the origins of topographic relief on Earth, Mars, and Titan

2
3 **Authors:** Benjamin A. Black^{1,2*}, J. Taylor Perron³, Douglas Hemingway⁴, Elizabeth Bailey⁵,
4 Francis Nimmo⁶, Howard Zebker⁷

5 6 **Affiliations:**

7 ¹ Department of Earth and Atmospheric Science, City College, City University of New York,
8 New York City, NY USA

9
10 ² Earth and Environmental Science, The Graduate Center, City University of New York, New
11 York City, NY USA

12
13 ³ Department of Earth, Atmospheric, and Planetary Sciences, Massachusetts Institute of
14 Technology, Cambridge, MA, USA

15
16 ⁴ Department of Earth and Planetary Science, University of California, Berkeley, Berkeley, CA,
17 USA

18
19 ⁵ Division of Geological and Planetary Sciences, California Institute of Technology, Pasadena,
20 CA, USA

21
22 ⁶ Department of Earth and Planetary Sciences, University of California, Santa Cruz, Santa Cruz,
23 CA, USA

24
25 ⁷ Department of Geophysics, School of Earth Sciences, Stanford University, Stanford, CA, USA
26

27 *Correspondence to: bblack@ccny.cuny.edu

28
29 **Abstract:** Rivers have eroded the topography of Mars, Titan, and Earth, creating diverse
30 landscapes. However, the dominant processes that generated topography on Titan (and to some
31 extent on early Mars) are not well known. We analyze drainage patterns on all three bodies to
32 show that large drainages—which record interactions between deformation and erosional
33 modification—conform significantly better to long-wavelength topography on Titan and Mars
34 than on Earth. We use a numerical landscape evolution model to demonstrate that short-
35 wavelength deformation causes drainage directions to diverge from long-wavelength topography,
36 as observed on Earth. We attribute the observed differences to ancient long-wavelength
37 topography on Mars, recent or ongoing generation of long-wavelength relief on Titan, and
38 creation of short-wavelength relief by plate tectonics on Earth.

39
40 **One Sentence Summary:** Global drainage patterns reveal differences in the origins and
41 evolution of topography on Earth, Mars, and Titan.
42

43 **Main Text:**

44
45 Increasingly detailed observations of rocky and icy bodies in our solar system reveal
46 dramatic diversity in surface topographic features. Plate tectonics has shaped topography
47 extensively on Earth, but on less tectonically active worlds like Mars (1-5), and icy worlds like
48 Titan and Pluto (6-8), the origins and history of the observed surface topography are varied and
49 in some cases unknown. Fluid erosion offers a means to probe the long-term evolution of
50 topography because drainage patterns interact with topography as it is uplifted and eroded (e.g.,
51 9). Fluid runoff has shaped the surfaces of at least three bodies in the solar system in the form of
52 liquid water on Earth and Mars (e.g., 10) and liquid hydrocarbons on Titan (e.g., 11, 12), thereby
53 inscribing a record of how the development of landscapes has differed on these three worlds.

54 Earth's topography is dominated by the dichotomy between continents and ocean basins;
55 most rivers drain from continental interiors to the ocean. However Earth's topography is also
56 shaped by deformation concentrated near plate boundaries, such as the formation of collisional
57 mountain ranges or volcanic arcs above subduction zones. These features can divert rivers as
58 they traverse continents and can thereby displace drainage divides towards active margins,
59 reshaping some of the planet's richest ecosystems in the process (13). Many terrestrial river
60 basins in tectonically active regions are continuously reorganized in response to changing
61 tectonic boundary conditions (9). As fluvial erosion (i.e., erosion by surface liquid flow)
62 competes with tectonic deformation to shape Earth's landscapes, global drainage patterns should
63 come to reflect a combination of long-wavelength, continent-scale topography and shorter-
64 wavelength features such as mountain ranges.

65 Large-scale topography on Mars was established more than 3.5 billion years ago in the
66 wake of the formation of Borealis Basin (4, 14) and the growth of the Tharsis volcanic rise (1).
67 Most fluvial activity likely occurred early in the planet's history (5, 10, 15). On Titan, sparse
68 impact craters and mountainous terrains attest to active modification of the surface (16), though
69 the age and origin of relief and the tempo of erosional modification remain to be determined
70 (11). We consider whether global drainage patterns differ on Earth and Mars as a result of their
71 divergent geologic and surface histories, and we explore the implications of that comparison for
72 Titan and other bodies where the erosional and tectonic history is largely unknown.

73 Our hypothesis is that on planets or moons where long-wavelength processes dominate
74 production of relief, drainages should generally flow parallel to the slope of the long-wavelength
75 topography, and the correlation should improve only marginally as the resolution of the
76 topography is refined. We term the agreement between drainage patterns and topography at a
77 given scale the drainage conformity with topography. In this context, we consider topography to
78 be long-wavelength if it spans at least 1/40th of the planetary circumference; that is, spherical
79 harmonics up to degree and order 20 (on Earth, ~1000 km). On bodies shaped by processes like
80 plate tectonics that generate relief at shorter wavelengths, we expect reduced correlation at long
81 wavelengths, with gradual improvement as shorter-wavelength features that deflect rivers are
82 included in the comparison. We further hypothesize that the timing of deformation and erosion
83 influences global drainage patterns. If the establishment of a planet's topography is followed by
84 a long period of tectonic quiescence, rivers will have more time to adjust to—and alter—that
85 topography, and drainage directions will conform better with the long-wavelength component of
86 the altered topography. On planets where tectonic deformation is more recent or more intense
87 than fluvial erosion, shorter-wavelength topography related to this deformation will have a
88 stronger influence on drainage directions, and long-wavelength conformity will be reduced.

89 To test these hypotheses, we compared global drainage patterns and long-wavelength
90 topography for Earth, Mars and Titan (Fig. 1). We focus on fluviably modified worlds, but we
91 expect volcanic, cryovolcanic, and other fluid-flow features on bodies such as Venus and Pluto
92 to leave similar signatures. We combined new and existing maps of drainages on Titan (11, 12),
93 Earth (17), and Mars (18) with spherical harmonic models for topography (19-22). We computed
94 two proxy metrics for drainage conformity with topography (Fig. S1). The first metric, the
95 downhill percentage ($%d$), represents the proportion of points along a river that are at higher
96 elevations than the next downstream point for a given point spacing and spherical harmonic
97 expansion of topography (Fig. 2A). As topographic resolution becomes finer—in this case, as
98 topography is expanded to higher spherical harmonic degrees— $%d$ should approach 100% for
99 active drainage networks since liquids in open channels flow downhill. The second metric, the
100 conformity factor (A), is defined as $A = \text{median}(\cos(\delta))$, where δ is the angle between the river
101 drainage direction and the downslope direction of the topographic expansion (Fig. 2B). Values of
102 A closer to 1 indicate better agreement between flow directions and long-wavelength topography,
103 but we do not expect perfect conformity ($A=1$) at any resolution because we are comparing the
104 steepest descent direction at a particular point to the flow direction across a finite interval.

105 Our results for topographic conformity as a function of maximum spherical harmonic
106 degree are shown in Fig. 2. Conformity is consistently lower on Earth than on Mars or Titan,
107 whereas Titan's conformity factor overlaps within uncertainty with that of Mars. The $%d$ values
108 are likewise much higher on Mars and Titan than on Earth. As expected, no body reaches near-
109 perfect topographic conformity at the long wavelengths we consider here. These results lead us
110 to the counterintuitive observation that many of Earth's rivers appear to flow sideways or uphill
111 with respect to long-wavelength topography (as shown in Fig. 1B at locations where river traces
112 deviate from gradient arrows), in contrast to most drainages on Titan and Mars.

113 On Mars, the strong correlation between valley network orientations and the present-day
114 long-wavelength topography requires that most large-scale topography predates valley network
115 formation in the Noachian era, and that this ancient topography was the dominant influence on
116 valley network orientation (Fig. 1F) (1, 2, 23). Martian topographic conformity remains
117 imperfect even when shorter wavelengths are considered (Fig. S5). We attribute this persistent,
118 moderate disagreement between drainage directions and topography to the combined effects of
119 impact cratering, topographic resolution, and deformation after the era of valley network
120 formation (24, 25). Because $%d$ quantifies the proportion of river segments that flow from higher
121 to lower topography (Fig. 2A and S5), our results place bounds on the amount of vertical
122 deformation after the era of valley network formation. For at least 85% of the fluviably dissected
123 landscapes on Mars, Hesperian and Amazonian era vertical deformation has not exceeded the
124 initial relief.

125 For Titan, a similar analysis suggests that mid-latitude and equatorial topography has
126 been stable since the formation of the fluvial networks. If present-day topography was shaped by
127 an episode of non-uniform crustal thickening at 0.3-1.2 Ga (16, 26), fluvial networks at middle
128 and low latitudes must have formed after that time. In contrast, many of Titan's north polar
129 networks deviate from regional gradients (Fig. S3). This result is consistent with recent or
130 ongoing predominantly short-wavelength deformation in the north polar region.

131 What processes have shaped the topographic conformity of Earth, Mars, and Titan?
132 Multiple factors could plausibly contribute to weak long-wavelength topographic conformity,
133 including little erosion relative to relief and resurfacing, low-amplitude long-wavelength
134 topography, impact cratering, or vigorous short-wavelength deformation. However, Earth is

135 deeply eroded, the topographic power spectra for the terrestrial planets are self-affine (i.e., the
136 height of relief features scales with their wavelength), and topographic power spectra for the
137 Earth and Mars are almost identical (20, 27). Consequently, neither weak erosion nor contrasts in
138 global static topography can fully explain the low topographic conformity on Earth relative to
139 Mars.

140 On Earth, plate tectonics preserves cratons—broad, flat regions where small changes in
141 topography can yield large shifts in conformity—while driving short-wavelength,
142 spatiotemporally variable rock uplift at active margins. To explore the influence of terrestrial
143 plate tectonics on drainage network evolution, we analyzed river network conformity for a series
144 of numerical landscape evolution model simulations (19, 28). We completed two sets of ten
145 idealized simulations: the first set with spatially uniform uplift to represent a world in which
146 long-wavelength deformation dominates the production of relief (Fig. 3A), and the second set
147 with spatially variable uplift to capture the effects of short wavelength deformation on drainage
148 orientations (Fig. 3B). The simulations with variable uplift are intended to investigate the
149 particular influence of plate tectonics. According to both our metrics, drainage directions in the
150 uniform uplift simulations conform much better with long-wavelength topography than in the
151 variable uplift simulations (Figs. 3C and 3D). The absolute magnitudes of A and $\%d$ are higher in
152 the model than in natural drainage networks, partly because the model lacks cratons and
153 sedimentary basins, both of which suppress conformity in nature. Nonetheless, our idealized
154 model offers qualitative insights into the effects of variable uplift on drainage patterns. Active,
155 spatially variable uplift depresses topographic conformity, but this effect is temporary: once the
156 variable uplift ceases, the topographic conformity steadily increases (Fig. S4A). Overall, the
157 results support our hypothesis that short-wavelength active deformation (such as mountain-
158 building on Earth) interferes with the background pattern of rivers draining the continents.

159 Geomorphic mapping shows that drainage basins on Mars are strongly influenced by pre-
160 existing ancient Noachian topography, including the hemispheric dichotomy, early Noachian
161 impact structures, and subtle ridges of unknown origin located throughout the southern highlands
162 (2, 23). Cratering during and after the ~ 4 Ga Late Heavy Bombardment further disrupted some
163 drainage basins (2, 23, 24). To quantify the extent of this disruption and the consequences for
164 topographic conformity, we conducted additional landscape evolution simulations (19). We find
165 that unless impacts obliterate drainages entirely, they can modify but do not erase alignment with
166 pre-existing long-wavelength topography (Fig. 4), consistent both with mapped relationships
167 between drainage patterns and large-scale slopes (1, 2, 23) and with our measurements showing
168 relatively high Martian topographic conformity. Crustal magnetization (29) and >3.6 Ga felsic
169 rocks on Mars (30) have been interpreted as evidence for processes typically associated with
170 plate tectonics on Earth. Our model results and the high conformity of Martian drainage
171 networks suggest that at the time of Martian river incision, plate tectonics was absent and impact
172 cratering was insufficiently intense to fully disrupt drainage alignment with ancient long-
173 wavelength topographic gradients (1, 2, 5, 23).

174 Of the three bodies we consider here, Titan's geologic history is the most enigmatic. In
175 contrast to the ancient long-wavelength topography of Mars (1, 4), Titan shows evidence for
176 recent or ongoing geologic activity (11, 16, 26). Titan's long-wavelength conformity thus
177 implies that long-wavelength mechanisms actively dominate the generation of relief in most
178 regions of Titan (the north polar region is a possible exception). A mechanism such as global-
179 scale changes in shell thickness due to tidal heating or basal melting and refreezing would create
180 both long-wavelength relief and local fractures on Titan (7, 31). Titan's high topographic

181 conformity supports geophysical arguments for significant sediment transfer from topographic
182 highs to lows (31). Patterns in Titan's atmospheric circulation are expected to result in net
183 poleward transport of hydrocarbons from mid-latitudes (32). Of the drainages we mapped on
184 Titan that are located poleward of 45 °N and 45 °S latitudes, and that traverse at least two
185 degrees of latitude, five out of six drain towards the poles (Fig. 1; Database S1). This implies that
186 other hydrocarbon fluxes or transport mechanisms must balance the net atmospheric and fluvial
187 transport of hydrocarbons toward Titan's poles.

188 Topographic conformity does not reach the near-perfect *%d* predicted by the model on
189 any of the three bodies we consider because of limited map resolution (19). Modest short-
190 wavelength deformation, impact cratering, or deformation after the development of drainages (5,
191 25) have probably also contributed to the imperfect conformity on Mars and Titan. The
192 improvement of drainage alignment on Earth relative to Mars at very short wavelengths (24)
193 supports this interpretation for Mars. In a set of landscape evolution simulations in which uplift
194 ceases entirely after a period of variable uplift, we find that topographic gradients on the
195 resulting low-relief surfaces (similar to Earth's cratons) can eventually grow weak and chaotic at
196 shorter wavelengths, allowing drainage patterns to retain the imprint of past conditions (Fig.
197 S4B). On Earth, topographic conformity dips at scales of 750-1500 km, which we attribute to
198 steep gradients in elevation from ocean basins to convergent margins to low-relief continental
199 interiors.

200 Earth and Mars share similarly bimodal topography (33) but divergent global geology,
201 proving that the distribution of elevations alone cannot reveal geologic evolution. The interaction
202 of rivers with long-wavelength topography provides an alternative record of the generation of
203 planetary relief. The formation and amalgamation of continental crust are processes that create
204 dominantly long wavelength topography, as is the process that built the Martian hemispheric
205 dichotomy. Construction of mountain ranges on Earth has a dominantly intermediate
206 wavelength, necessarily smaller than the scale of continents. Martian drainage patterns reflect
207 ancient long-wavelength topography that predates both valley network formation and Noachian-
208 Hesperian bombardment (2), confirming that Noachian Mars lacked global plate tectonics and
209 bounding post-Noachian changes in Martian relief. Our results favor dominantly long-
210 wavelength relief-generating mechanisms on Titan such as shell thickness variations arising from
211 tidal heating (6, 7) or thermal expansion and contraction (6). Together, the three river-worn
212 bodies in our solar system provide a Rosetta stone for deciphering the imprint of tectonics on
213 landscapes.

214
215
216
217
218

219 **References**

- 220 1. R. J. Phillips *et al.*, Ancient geodynamics and global-scale hydrology on Mars. *Science*. **291**, 2587-
221 2591 (2001).
- 222 2. R. P. Irwin, A. D. Howard, Drainage basin evolution in Noachian Terra Cimmeria, Mars. *Journal of*
223 *Geophysical Research: Planets*. **107**(2002).
- 224 3. J. T. Perron, J. X. Mitrovica, M. Manga, I. Matsuyama, M. A. Richards, Evidence for an ancient
225 martian ocean in the topography of deformed shorelines. *Nature*. **447**, 840-843 (2007).
- 226 4. J. C. Andrews-Hanna, M. T. Zuber, W. B. Banerdt, The Borealis basin and the origin of the martian
227 crustal dichotomy. *Nature*. **453**, 1212-1215 (2008).
- 228 5. S. Bouley *et al.*, Late Tharsis formation and implications for early Mars. *Nature*.(2016).
- 229 6. G. C. Collins *et al.*, Tectonics of the outer planet satellites. *Planetary Tectonics*. **11**, 264 (2009).
- 230 7. F. Nimmo, B. Bills, Shell thickness variations and the long-wavelength topography of Titan. *Icarus*.
231 **208**, 896-904 (2010).
- 232 8. J. M. Moore *et al.*, The geology of Pluto and Charon through the eyes of New Horizons. *Science*. **351**,
233 1284-1293 (2016).
- 234 9. S. D. Willett, S. W. McCoy, J. T. Perron, L. Goren, C. Chen, Dynamic Reorganization of River Basins.
235 *Science*. **343**(2014).
- 236 10. A. D. Howard, J. M. Moore, R. P. Irwin, An intense terminal epoch of widespread fluvial activity on
237 early Mars: 1. Valley network incision and associated deposits. *Journal of Geophysical Research: Planets*
238 (1991–2012). **110**(2005).
- 239 11. B. A. Black, J. T. Perron, D. M. Burr, S. A. Drummond, Estimating erosional exhumation on Titan
240 from drainage network morphology. *Journal of Geophysical Research*. **117**, E08006 (2012).
- 241 12. D. M. Burr, S. A. Drummond, R. Cartwright, B. A. Black, J. T. Perron, Morphology Of Fluvial
242 Networks On Titan: Evidence For Structural Control. *Icarus*. **226**, 742-759 (2013).
- 243 13. C. Hoorn *et al.*, Amazonia through time: Andean uplift, climate change, landscape evolution, and
244 biodiversity. *Science*. **330**, 927-931 (2010).
- 245 14. H. V. Frey, J. H. Roark, K. M. Shockey, E. L. Frey, S. E. Sakimoto, Ancient lowlands on Mars.
246 *Geophys. Res. Lett.* **29**(2002).
- 247 15. C. I. Fassett, J. W. Head, The timing of martian valley network activity: Constraints from buffered
248 crater counting. *Icarus*. **195**, 61-89 (2008).
- 249 16. C. D. Neish, R. D. Lorenz, Titan’s global crater population: A new assessment. *Planetary and Space*
250 *Science*. **60**, 26-33 (2012).

251 17. H. Wu *et al.*, A new global river network database for macroscale hydrologic modeling. *Water*
252 *Resources Research*. **48**, W09701 (2012).

253 18. B. M. Hynek, M. Beach, M. R. Hoke, Updated global map of Martian valley networks and
254 implications for climate and hydrologic processes. *Journal of Geophysical Research: Planets (1991–*
255 *2012)*. **115**(2010).

256 19. Materials and methods are available as supplementary materials on Science Online.

257 20. M. A. Wieczorek, Gravity and Topography of the Terrestrial Planets. *Treatise on Geophysics*. **10**,
258 153-193 (2015).

259 21. H. A. Zebker *et al.*, Size and Shape of Saturn's Moon Titan. *Science*. **324**, 921-923 (2009).

260 22. C. Hirt, M. Kuhn, W. Featherstone, F. Göttl, Topographic/isostatic evaluation of new-generation
261 GOCE gravity field models. *Journal of Geophysical Research: Solid Earth (1978–2012)*. **117**(2012).

262 23. R. P. Irwin, R. A. Craddock, A. D. Howard, H. L. Flemming, Topographic influences on development
263 of Martian valley networks. *Journal of Geophysical Research: Planets*. **116**(2011).

264 24. W. Luo, T. Stepinski, Orientation of valley networks on Mars: The role of impact cratering. *Geophys.*
265 *Res. Lett.* **39**(2012).

266 25. A. Lefort, D. M. Burr, F. Nimmo, R. E. Jacobsen, Channel slope reversal near the Martian dichotomy
267 boundary: Testing tectonic hypotheses. *Geomorphology*.(2014).

268 26. G. Tobie, J. I. Lunine, C. Sotin, Episodic outgassing as the origin of atmospheric methane on Titan.
269 *Nature*. **440**, 61-64 (2006).

270 27. D. L. Turcotte, A fractal interpretation of topography and geoid spectra on the Earth, Moon, Venus,
271 and Mars. *Journal of Geophysical Research: Solid Earth (1978–2012)*. **92**, E597-E601 (1987).

272 28. J. T. Perron, W. E. Dietrich, J. W. Kirchner, Controls on the spacing of first-order valleys. *Journal of*
273 *Geophysical Research-Earth Surface*. **113**(2008).

274 29. F. Nimmo, D. Stevenson, Influence of early plate tectonics on the thermal evolution and magnetic
275 field of Mars. *Journal of Geophysical Research: Planets (1991–2012)*. **105**, 11969-11979 (2000).

276 30. V. Sautter *et al.*, In situ evidence for continental crust on early Mars. *Nature Geoscience*. **8**, 605-609
277 (2015).

278 31. D. Hemingway, F. Nimmo, H. Zebker, L. Iess, A rigid and weathered ice shell on Titan. *Nature*. **500**,
279 550-552 (2013).

280 32. T. Schneider, S. D. B. Graves, E. L. Schaller, M. E. Brown, Polar methane accumulation and
281 rainstorms on Titan from simulations of the methane cycle. *Nature*. **481**, 58-61 (2012).

282 33. R. D. Lorenz *et al.*, Hypsometry of Titan. *Icarus*. **211**, 699-706 (2011).

283 34. B. W. Stiles *et al.*, Determining Titan surface topography from Cassini SAR data. *Icarus*. **202**, 584-
284 598 (2009).

285 35. H. Zebker *et al.*, Titan's Figure Fatter, Flatter Than Its Gravity Field. *AGU Fall Meeting*
286 *Abstracts*.(2012).

287 36. L. Iess *et al.*, The tides of Titan. *Science*. **337**, 457-459 (2012).

288 37. D. E. Smith *et al.*, The global topography of Mars and implications for surface evolution. *Science*.
289 **284**, 1495-1503 (1999).

290 38. D. Smith, G. Neumann, R. Arvidson, E. Guinness, S. Slavney, Mars Global Surveyor laser altimeter
291 mission experiment gridded data record. *NASA Planetary Data System*.(2003).

292 39. J. T. Perron, J. W. Kirchner, W. E. Dietrich, Formation of evenly spaced ridges and valleys. *Nature*.
293 **460**, 502-505 (2009).

294 40. A. D. Howard, G. Kerby, Channel changes in badlands. *Geological Society of America Bulletin*. **94**,
295 739-752 (1983).

296 41. K. L. Ferrier, K. L. Huppert, J. T. Perron, Climatic control of bedrock river incision. *Nature*. **496**,
297 206-209 (2013).

298 42. K. X. Whipple, G. E. Tucker, Dynamics of the stream-power river incision model: Implications for
299 height limits of mountain ranges, landscape response timescales, and research needs. *Journal of*
300 *Geophysical Research-Solid Earth*. **104**, 17661-17674 (1999).

301 43. S. D. Willett, Orogeny and orography: The effects of erosion on the structure of mountain belts.
302 *Journal of Geophysical Research: Solid Earth*. **104**, 28957-28981 (1999).

303 44. C. Vörösmarty, B. Fekete, M. Meybeck, R. Lammers, Global system of rivers: Its role in organizing
304 continental land mass and defining land-to-ocean linkages. *Global Biogeochem. Cycles*. **14**, 599-621
305 (2000).

306 45. C. J. Barnhart, A. D. Howard, J. M. Moore, Long-term precipitation and late-stage valley network
307 formation: Landform simulations of Parana Basin, Mars. *Journal of Geophysical Research: Planets*.
308 **114**(2009).

309 46. E. S. Kite, A. Lucas, C. I. Fassett, Pacing early Mars river activity: Embedded craters in the Aeolis
310 Dorsa region imply river activity spanned \geq (1–20) Myr. *Icarus*. **225**, 850-855 (2013).

311 47. B. A. Ivanov, Mars/Moon cratering rate ratio estimates. *Space Science Reviews*., 87-104 (2001).

312 48. S. T. Stewart, G. J. Valiant, Martian subsurface properties and crater formation processes inferred
313 from fresh impact crater geometries. *Meteoritics & Planetary Science*. **41**, 1509-1537 (2006).

314 49. N. K. Forsberg-Taylor, A. D. Howard, R. A. Craddock, Crater degradation in the Martian highlands:
315 Morphometric analysis of the Sinus Sabaeus region and simulation modeling suggest fluvial processes.
316 *Journal of Geophysical Research: Planets*. **109**(2004).

317 50. N. Mangold *et al.*, The origin and timing of fluvial activity at Eberswalde crater, Mars. *Icarus*. **220**,
318 530-551 (2012).

319 51. B. M. Hynek, R. J. Phillips, New data reveal mature, integrated drainage systems on Mars indicative
320 of past precipitation. *Geology*. **31**, 757-760 (2003).

321 52. D. G. Tarboton, A new method for the determination of flow directions and upslope areas in grid
322 digital elevation models. *Water Resour. Res.* **33**, 309-319 (1997).

323 53. W. J. Conover, W. Conover, *Practical nonparametric statistics* (Wiley and Sons, New York, NY,
324 1980).

325 54. M. Longnecker, R. Ott, *An introduction to statistical methods and data analysis* (Nelson Education,
326 Toronto, Canada, 2001).

327 55. W. H. Smith, D. T. Sandwell, Global sea floor topography from satellite altimetry and ship depth
328 soundings. *Science*. **277**, 1956-1962 (1997).

329

330

331

332

333 **Acknowledgments:** We thank Erik Chan for spot-checking Martian drainages. Three reviewers
334 provided constructive feedback. BAB acknowledges NASA grant NNX16AR87G. We thank the
335 Cassini team. The landscape evolution code Tadpole is available on GitHub.

336

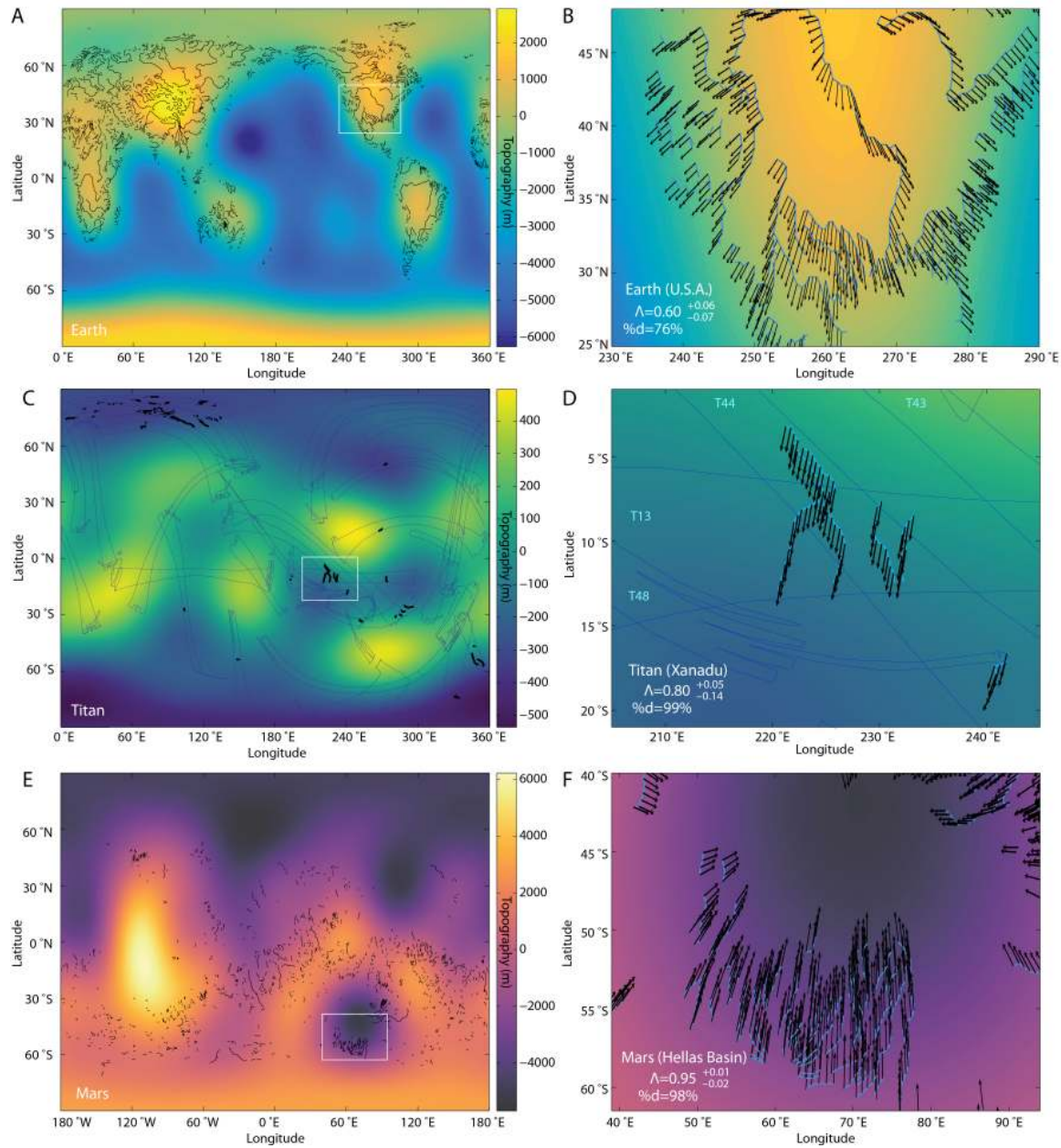


Fig. 1. Maps of topography referenced to the geoid and expanded to spherical harmonic degree and order 6, overlain with the fluvial features employed in this study. (A) Earth. (B) Enlargement of North America. (C) Titan. Blue outlines show Cassini Synthetic Aperture Radar observation swaths. (D) Enlargement of eastern Shangri-La and Xanadu regions of Titan. (E) Mars. (F) Enlargement of Hellas Basin on Mars. In A, C, E, white boxes outline regions enlarged in B, D, and F, where river courses are shown in blue; black arrows indicate topographic gradient at each point; and indicated conformity values span these enlarged regions, with uncertainties corresponding to the 95% confidence interval for the median.

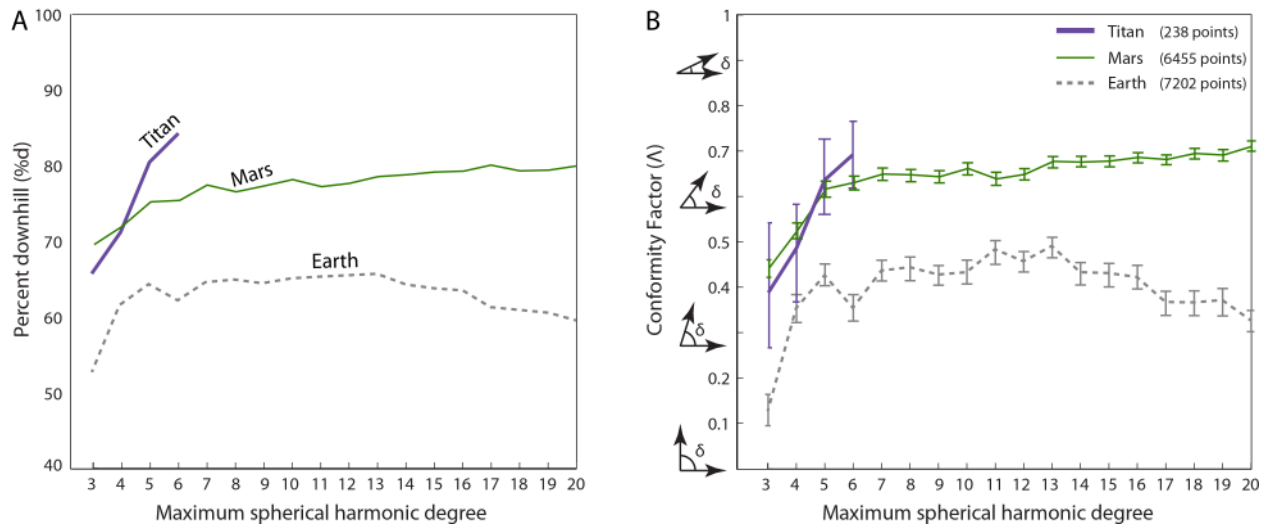


Fig. 2. Topographic conformity differs on Titan and Mars versus Earth. (A) The percent downhill ($\%d$) metric as a function of the spatial resolution of the spherical harmonic expansion. **(B)** The conformity factor [$\Lambda = \text{median}(\cos(\delta))$]. Angles corresponding to Λ values illustrated on vertical axis. Uncertainties correspond to the 95% confidence interval for the median (19).

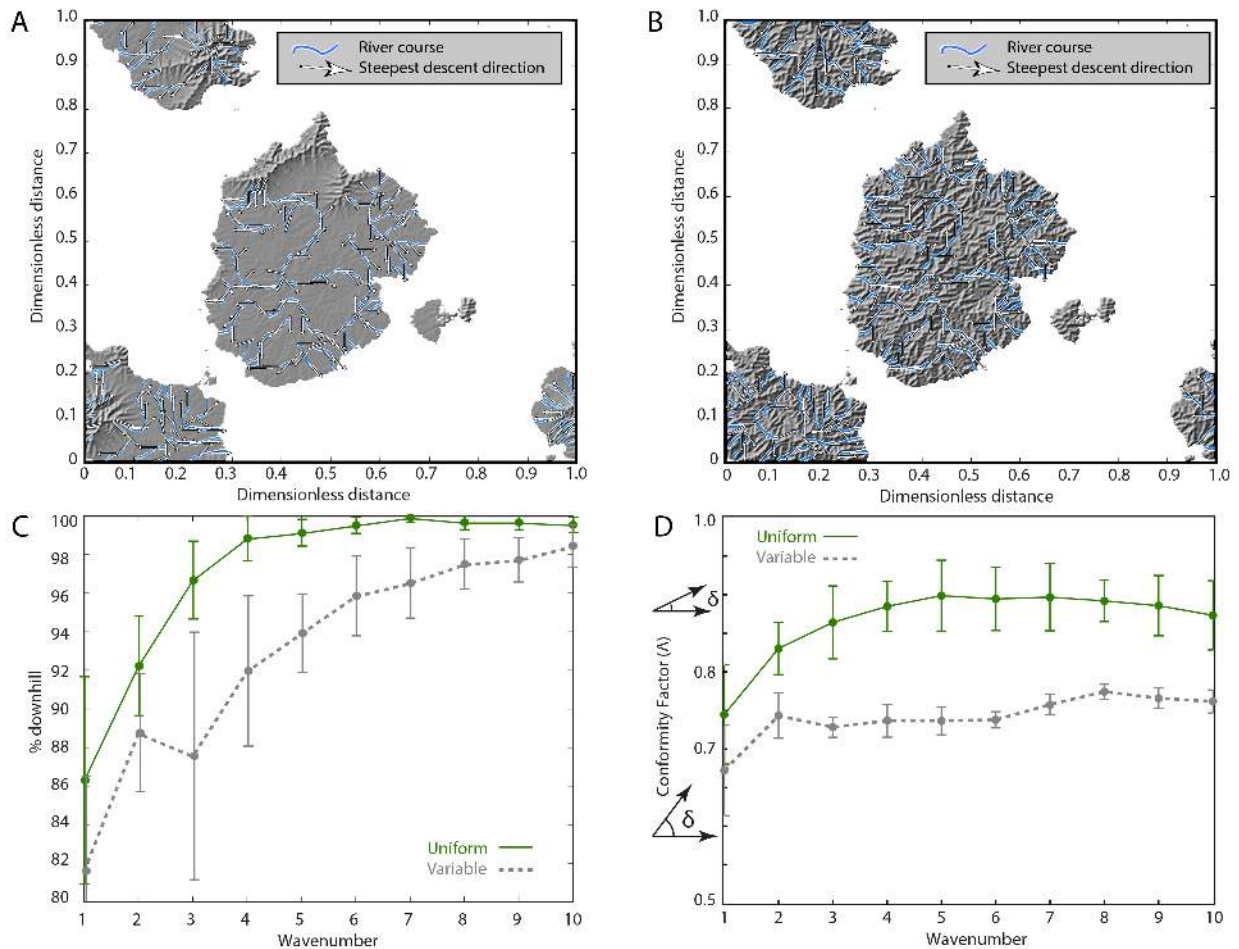


Fig. 3. Deformation history influences conformity. Variable uplift simulations (**A**) represent plate tectonic-style uplift; uniform uplift simulations (**B**) represent dominantly long-wavelength deformation. Shaded relief maps in **A** and **B** show simulations after 10 Myr. The model domain is doubly periodic, and the lowest 70% of initial elevations (white) were set as the base level relative to which uplift occurs. (**C**) Mean % downhill among 10 variable uplift simulations and 10 uniform uplift simulations. (**D**) Mean topographic conformity among the same simulations analyzed in **C**. In **C** and **D**, error bars represent two standard errors of the mean across the simulation ensembles.

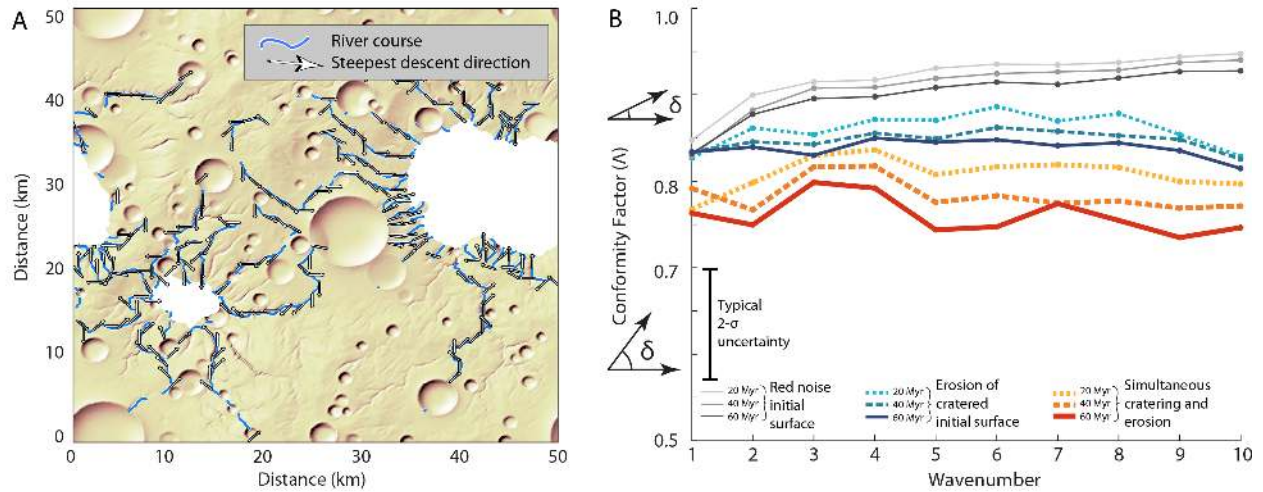


Fig. 4. Impact cratering can modulate topographic conformity. (A) Shaded relief map of a representative simulation after 60 Myr erosion in tandem with impact cratering. (B) Mean topographic conformity among 10 control simulations, 10 simulations with a cratered initial surface, and 10 simulations with ongoing cratering in tandem with fluvial erosion. Times refer to model time after initiation(19). Legend shows a typical uncertainty of two standard errors of the mean within the simulation ensembles.

344 **Supplementary Materials:**

345 Materials and Methods

346 Figures S1-S8

347 Tables S1 and S2

348 Database S1

349 References (34-55)

350

351
352
353
354
355
356
357
358
359
360
361
362
363
364
365
366
367
368
369
370
371
372
373
374
375
376
377

Supplementary Materials for

Global drainage patterns and the origins of topographic relief on Earth, Mars, and Titan

Benjamin A. Black, J. Taylor Perron, Douglas Hemingway, Elizabeth Bailey, Francis Nimmo, Howard Zebker

Correspondence to: bblack@ccny.cuny.edu

This PDF file includes:

Materials and Methods
Figs. S1 to S8
Table S1 and S2
Caption for database S1

Other Supplementary Materials for this manuscript include the following:

Database S1 as .xlsx file

378 **Materials and Methods**

379 Our work relies on three principal datasets: maps of fluvial features on Titan, Earth, and Mars;
380 spherical harmonic models for the topography of each of these bodies; and results from a
381 numerical model of landscape evolution under a range of uplift conditions. We outline our
382 methods for each dataset below.

383

384 Mapping fluvial features

385

386 *Earth.* To identify major fluvial features on Earth, we used 1/8th degree grids of global flow
387 accumulation, basins, and flow length derived from orbital altimetry and corrected manually
388 (17). We identified each sink as a point of maximum flow accumulation within each basin, and
389 the main trunk as the flow path linking each sink to the most distant point (along flow paths)
390 within each basin. For rivers that spanned more than ~50 km, we identified sampling points at an
391 interval of ~50 km, or every 5th grid point (the results are relatively insensitive to this selection;
392 we chose this interval because it was sufficiently large to avoid sensitivity to the 1/8th degree
393 resolution of the drainage dataset). We analyzed only rivers longer than this 50 km interval.

394

395 *Mars.* We relied on a global database of Martian river networks (18). Sinks were identified as the
396 topographically lowest extremities within each network; the validity of these sinks was spot-
397 checked visually. The main trunk of each network was taken to be the path linking the most
398 distal point within a network to the sink. We identified sampling points along this main trunk at
399 an interval that matches the interval we used on Earth, but scaled by the ratio
400 $\text{Radius}_{\text{Mars}}/\text{Radius}_{\text{Earth}}$ (this interval equates to ≈ 30 km on Mars). We analyzed only networks
401 longer than this interval.

402

403 *Titan.* We manually selected 71 drainage networks from a global database compiled from the
404 Cassini spacecraft's Synthetic Aperture Radar (SAR) swaths Ta to T71 (12). These drainages
405 were delineated on the basis of: i) linear geometry cross-cutting other SAR features; ii) light-dark
406 pairings indicative of narrow topographic features; iii) branching geometries; iv) drainage into
407 features interpreted as lakes (11, 12). We selected drainages where we could confidently identify
408 a sink location on the basis of junction angles, progressive downstream widening of valley
409 features, orientation relative to features interpreted as lakes, and/or locally available stereo
410 topography (34). The source and sink coordinates we identified for all 71 networks we analyzed
411 on Titan are given in Database S1. The main trunk of each network was taken to be the path
412 linking the most distant point within a network to the sink. We identified sampling points along
413 this main trunk at an interval that matches the interval we used on Earth, but scaled by the ratio
414 $\text{Radius}_{\text{Titan}}/\text{Radius}_{\text{Earth}}$ (this interval equates to ≈ 21 km on Titan). We analyzed only networks
415 longer than this interval. We defined a subset of North Polar networks as all eligible drainages
416 with sinks located north of 60 °N latitude.

417

418 Spherical harmonic topography

419

420 We constructed spherical harmonic models of topography for Titan from RADAR-based
421 topography (21, 31, 35) referenced to the geoid (36); for Earth from the Earth2012
422 topography/bathymetry model (referenced to sea level) (22); and for Mars from the Mars Orbiter

423 Laser Altimeter (MOLA)-derived, aeroid-referenced topography model (37, 38). A robust
424 spherical harmonic expansion for Titan’s topography is available only up to degree (ℓ) 6 (ref.
425 (21)). Titan has less long-wavelength relief than Earth or Mars (Fig. 1), indicating that the
426 magnitude of topography alone cannot explain conformity. Our spherical harmonic models of
427 terrestrial topography include bathymetry (Fig. S6). Oceanic basins form an integral part of
428 Earth’s plate tectonically derived topography (though the weight of the oceans deepens ocean
429 basins, and fluvial erosion does not operate on the seafloor). Ancient oceans may also once have
430 existed on Mars (3).

431

432 Data availability

433

434 Coordinates for all drainage networks analyzed on Titan are available in spreadsheet form in
435 Database S1. The data required to generate spherical harmonic topography for Earth, Titan, and
436 Mars are available from the references provided in the text.

437

438 Landscape evolution model

439

440 Our landscape evolution model considers the effects of fluvial incision, uplift, and hill slope
441 erosion (parameterized with a critical slope) on surface topography (11, 28, 39). The model is
442 available at <https://github.com/MITGeomorph/Tadpole>.

443

444 *Variable vs. uniform uplift.* The landscape evolution model solves the stream-power equation for
445 the time evolution of fluvially eroded topography(28, 39):

446

$$\frac{dz}{dt} = U - KA^m |\nabla z|^n \quad (S1)$$

447

448 with elevation z , contributing area A , stream-power coefficient K , rate of uplift relative to a
449 boundary U , m a constant taken to be 0.5(40), and n a constant taken to be 1 (41). Hill slope
450 processes, which occur at finer scales than are of interest for comparison with our global
451 topographic models, are approximated with a critical slope of 0.6, which prevents slopes from
452 becoming unrealistically steep at drainage divides (11).

453 The power-law relationship between incision rate and channel slope and contributing
454 drainage area in Eq. (1) can be derived from the assumption that channel erosion rates scale with
455 bed shear stress due to flow in a channel (28, 40), and is motivated by the observed negative
456 correlation between channel slope and contributing drainage area on Earth (42). In our
457 simulations, we assume a spatially constant stream-power coefficient, though in practice climatic
458 and lithologic variations can lead to spatial variability in K (41). Plate tectonics produces a
459 patchwork of continental lithologies, and the orogenic feedback loop links mountain-building,
460 exhumation, and climate (43). The first effect might be expected to prolong the effects of plate
461 tectonics in suppressing topographic conformity even after active deformation has ceased; the
462 second effect might be expected to complicate the relationship between rock uplift, topography,
463 and drainage patterns.

464 We derive a non-dimensional form of the governing equation following (28):

465

$$\frac{dz'}{dt'} = \frac{KL^{2m}}{U} A'^m |\nabla' z'| + 1 \quad (\text{S2})$$

466 with $z = z' L$, $A = A' L^2$, $t = t' L/U$, $\nabla = \nabla' / L$. The lengthscale L is chosen to represent the
 467 distance from the drainage divide to the sink.
 468

469 We initialize our simulations with randomly generated, autocorrelated initial topography;
 470 the lowest 70% of the initial surface is set to be a topographic sink as an analog for Earth's
 471 oceans (Fig. S7). We tabulate model parameter values in Table S1. In the simulations we
 472 analyzed, $13 \pm 12\%$ (1σ) of the land area is internally drained. For comparison, $14 \pm 10\%$ (1σ ;
 473 the uncertainty reflects variability across continents) of Earth's unglaciated land area is internally
 474 drained (44). To approximate the effects of plate tectonics, which localizes crustal thickening,
 475 the variable uplift cases have a pseudo-random pattern of autocorrelated, spatially non-uniform
 476 uplift superposed on the background uniform uplift field.

477 In place of spherical harmonic decompositions to characterize the model topography, we
 478 used 2-D Fourier transforms as described below.
 479

480 *Impact cratering.* Impact cratering is one of the key mechanisms for relief generation on Mars.
 481 Crater counting of fluvial landscapes suggests that river activity reached a climax around the
 482 Noachian-Hesperian boundary, followed by a decline in activity that roughly coincided with
 483 waning cratering activity after the Late Heavy Bombardment (10, 15). Landscape evolution
 484 modeling and crater counting further suggests that the terminal period of relatively intense
 485 fluvial activity lasted at least 10^3 - 10^4 years, and more likely spanned 10^5 - 10^7 years of episodic
 486 activity (45, 46). Ancient large-scale topography on Mars, including the hemispheric dichotomy,
 487 predates fluvial incision (1, 5). This topography may have been generated through basin-scale
 488 impacts (4) or through other unknown processes. Geomorphic mapping suggests that valley
 489 networks were strongly influenced by ancient topographic gradients, but that younger Noachian-
 490 Hesperian cratering did modify and disrupt some river paths (2, 23).

491 To investigate and quantify the influence of impact cratering on topographic conformity,
 492 we ran three landscape evolution model ensembles, each with ten simulations (Fig. S8), in which
 493 we considered (i) an initial surface with randomly generated, autocorrelated initial topography
 494 (our control ensemble, which represents ancient topography without any younger, fresh craters),
 495 (ii) an initial surface with randomly generated, autocorrelated topography, with superposed
 496 impact craters (to represent erosion of ancient topography that has experienced more recent
 497 cratering), (iii) an initial surface with randomly generated, autocorrelated topography, with
 498 superposed impact craters, and with additional impact cratering occurring in tandem with fluvial
 499 erosion (to represent cratered, ancient topography that undergoes fluvial erosion in tandem with
 500 cratering, for example during the Late Heavy Bombardment).

501 To account for the greater occurrence of smaller craters, we assumed the size-frequency
 502 distribution for Martian impact craters as adapted from the lunar production function for craters
 503 1-16 km in diameter (47). The autocorrelated initial topography represents ancient topography,
 504 for example due to basin-forming impacts. However, we did not generate fresh craters larger
 505 than 16 km diameter, because our goal was to study the interaction of impacts with pre-existing
 506 topography and valley networks (and larger impacts obliterate both for our chosen grid size of 50
 507 km by 50 km). We used scaling relationships for Mars highland craters (48) to calculate crater
 508 depths for the strength and gravity regimes, and we employed polynomial fits from (48) to
 509 calculate the shapes of axisymmetric cavities, rims, and uplift zones. Following (49), we

510 calculated the final topography outside the crater rim as a weighted average of the pre-impact
511 topography and the impact-generated topography, where the weighting declines linearly from the
512 rim to a distance of three radii from the crater center.

513 Our simulations to investigate impact cratering differ from those designed to investigate
514 the effects of plate tectonic-style deformation in that for the purposes of accurate impact crater
515 depth-diameter scaling, we have chosen to make these simulations dimensional. We used model
516 grids that represented lateral dimensions of 50 km by 50 km, with 125 meter horizontal
517 resolution. The complete list of parameters and parameter values used in the impact cratering
518 simulations is given in Table S2. The true duration and rate of valley network incision on Mars
519 are unknown (10, 50), and the rate and duration trade off in the model to determine the total
520 amount of incision. Trunk channels of Martian valley networks incised ~50 to 350 m into older
521 terrains (10), creating drainage densities of $\sim 10^{-2} \text{ km}^{-1}$ (51). We selected values for K (see Table
522 S2) and simulation duration (60 Myr) that generated cumulative erosion that qualitatively
523 matched typical values of drainage density and trunk channel fluvial incision observed on Mars.

524

525 Analysis

526

527 The metrics we applied to compare drainage orientations with topography are illustrated
528 graphically in Fig. S1. To avoid the need to weight fluvial features by size, and to integrate
529 changes in flow direction and downslope direction along river courses, we performed both the
530 %d and Λ analyses at intervals along the main trunks of major fluvial features (see Fig. S1).

531

532 *Synthetic networks.* The maximum size of observed drainage networks differs on Titan, Earth,
533 and Mars, which might a priori influence the scale of topography reflected in drainage
534 orientations. To avoid scale dependence in our comparison, we used a point spacing that is
535 uniform relative to planetary radius on each body. To test whether our algorithm displays any
536 bias related to drainage network scale, and to investigate the likelihood of false positive results,
537 we repeated our analyses on synthetic datasets. These datasets comprised line segments of
538 uniform length distributed and oriented randomly across the simulated landscape (Fig. S2). We
539 generated 1,000-10,000 such synthetic segments for each test, and we analyzed the portion of
540 those synthetic segments that crossed the landmasses in our simulations. In total, we conducted
541 four tests on representative simulations from the ensemble analyzed in the manuscript: with line
542 segments spanning either 1/2 or 1/20 the domain of our numerical simulations, and on
543 landscapes in which our simulations included either uniform or variable uplift. In all cases, our
544 analysis yielded statistically indistinguishable results with a topographic conformity of zero (Fig.
545 S2, panels E-F). In other words, the random synthetic networks showed no preferred orientation
546 relative to the topography, and our algorithm displayed no measureable bias due to systematic
547 differences in drainage size. These tests support the robustness of our results for Titan, Earth, and
548 Mars.

549

550 *Downhill percentage (%d).* At each upstream-downstream pair of sampling points along each
551 drainage path, we determined whether the upstream point is at a higher elevation according to the
552 topographic model at a given maximum degree. For each body (and each model run) %d is the
553 percentage of all upstream-downstream pairs that pass (i.e. the upstream point has a higher
554 elevation according to the model topography). At infinite resolution (or as wavenumber $k \rightarrow 200$

555 for the 400×400 model grids), %d should approach 100%, because liquid flows downhill with
556 respect to the geoid.

557

558 *Topographic conformity (A)*. At each sampling point along each drainage path, we determined δ ,
559 the angle between the steepest descent direction and the flow direction. For the planetary bodies,
560 steepest descent was determined using MATLAB's `gradient` function for the gradient on
561 spheroidal bodies; for the model runs, steepest descent was calculated according to the D-infinity
562 flow routing algorithm(52). We calculated flow direction as the azimuth of the vector linking
563 each sampling point to the next downstream point. We defined the topographic conformity at a
564 given maximum spherical harmonic degree or wavenumber as the median value of $\cos(\delta)$
565 calculated at all sampling points: $A_\ell = \text{median}(\cos(\delta))$.

566

567 *Uncertainties*. The uncertainties indicated in Figure 1, 2, S2, and S3 represent the 95%
568 confidence interval for the median. The 95% confidence interval for the median is bounded by
569 the j th and k th observation in a ranked list of n observations, where (53, 54):

570 $j = n \times q - 1.96 \sqrt{n \times q (1 - q)}$, and $k = n \times q + 1.96 \sqrt{n \times q (1 - q)}$.

571 Here $q = 0.5$, because by definition the median divides the dataset into two quantiles.

572

573 The uncertainties in Figure 3 represent two standard errors of the mean %d (Figure 3c)
574 and A (Figure 3d) values across the ensemble of ten simulations with spatially variable uplift and
575 ten simulations with spatially uniform uplift.

576

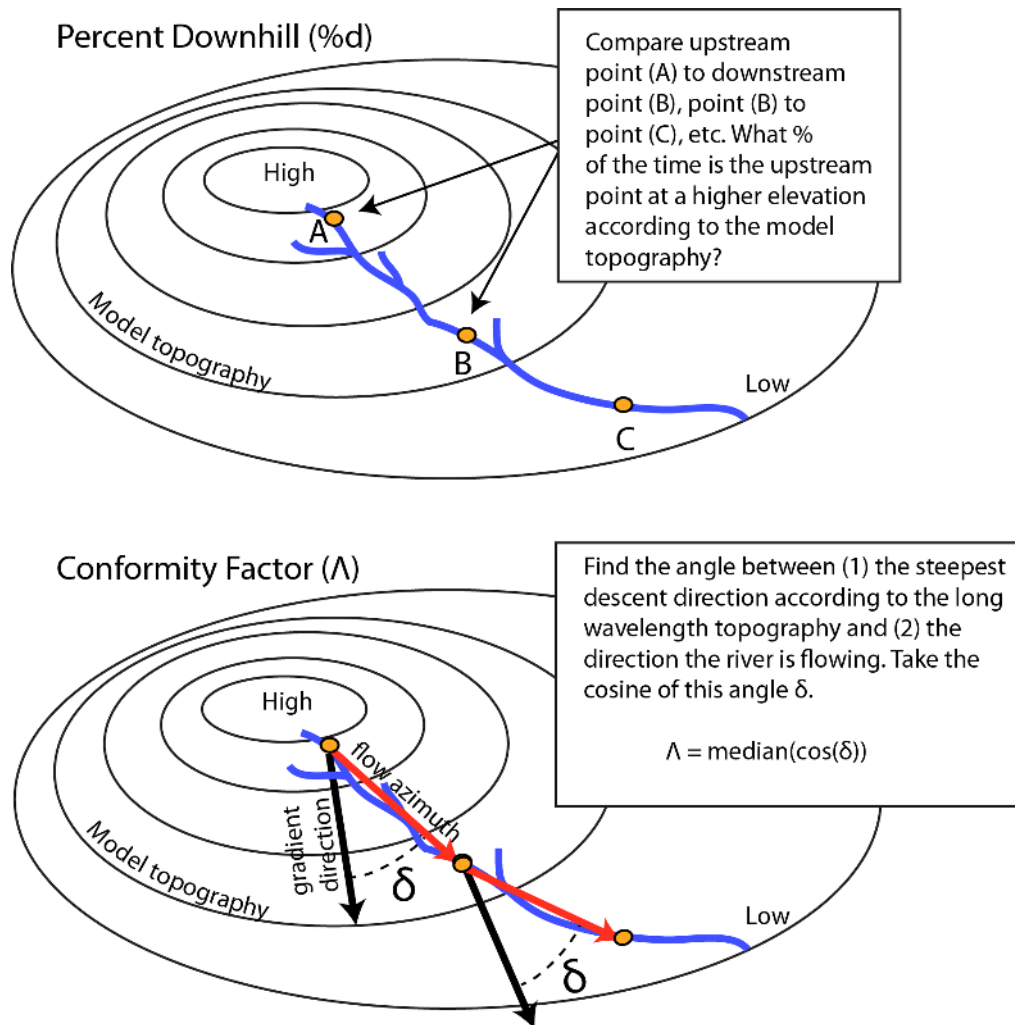


Fig. S1. Schematic illustration of two proxy metrics for the agreement between river orientations and topography at a given scale. The upper panel illustrates the definition of the percent downhill metric ($\%d$) and the lower panel the definition of the conformity factor (Λ).

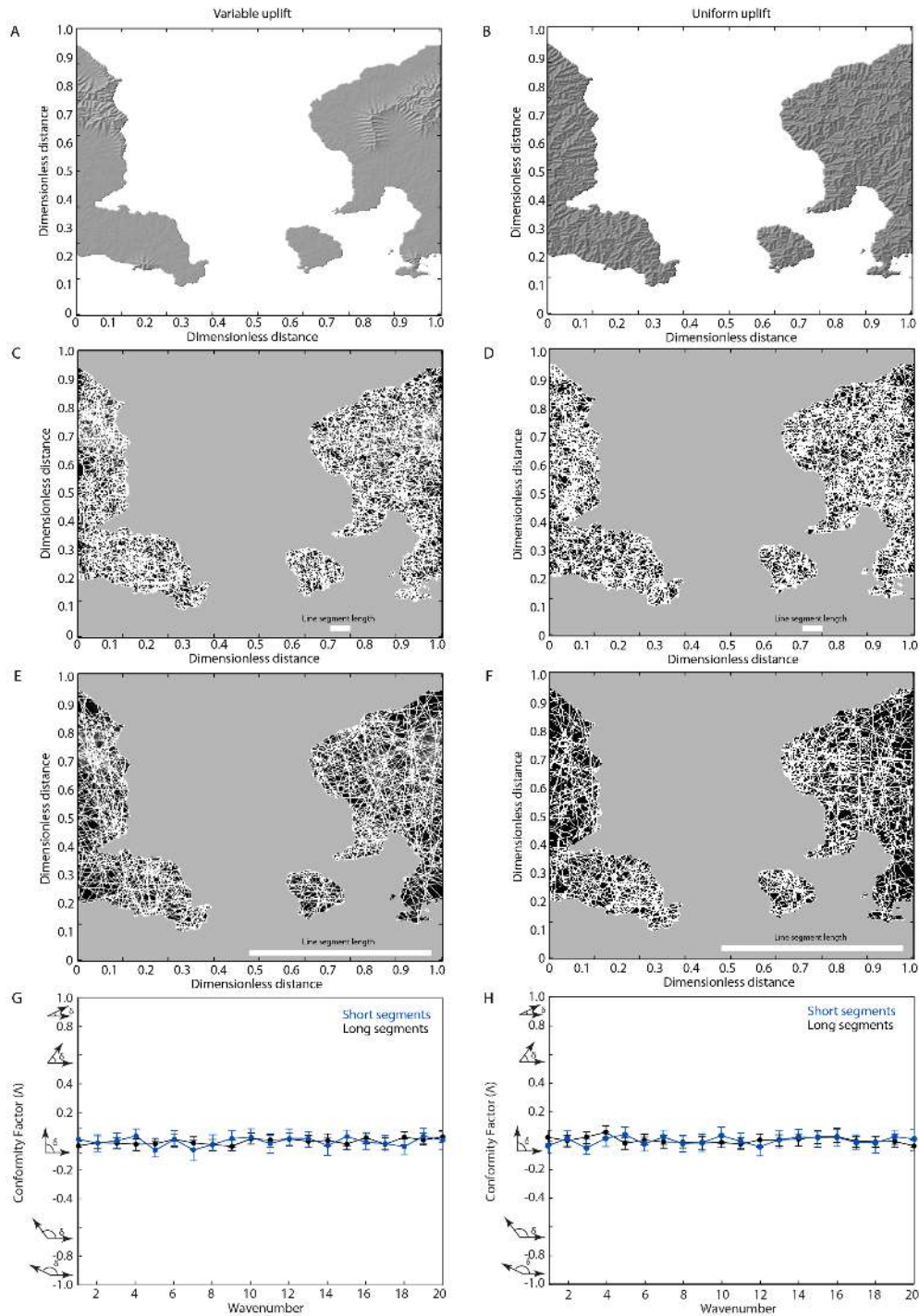


Fig. S2. Synthetic tests to identify any bias related to the scale of measured drainages. (A) Shaded relief map of model topography produced with spatially variable uplift. **(B)** As in A, but for spatially uniform uplift. **(C)** Short synthetic drainages, superposed on outline of topography from A. **(D)** As in C, but with spatially uniform uplift from B. **(E)** As in C, but with long synthetic drainages **(F)** As in E, but for uniform uplift. **(G)** Topographic conformity Λ for synthetic dataset with spatially variable uplift. **(H)** Topographic conformity Λ for synthetic dataset with spatially uniform uplift. Error bars correspond to the 95% confidence interval for the median.

580
581

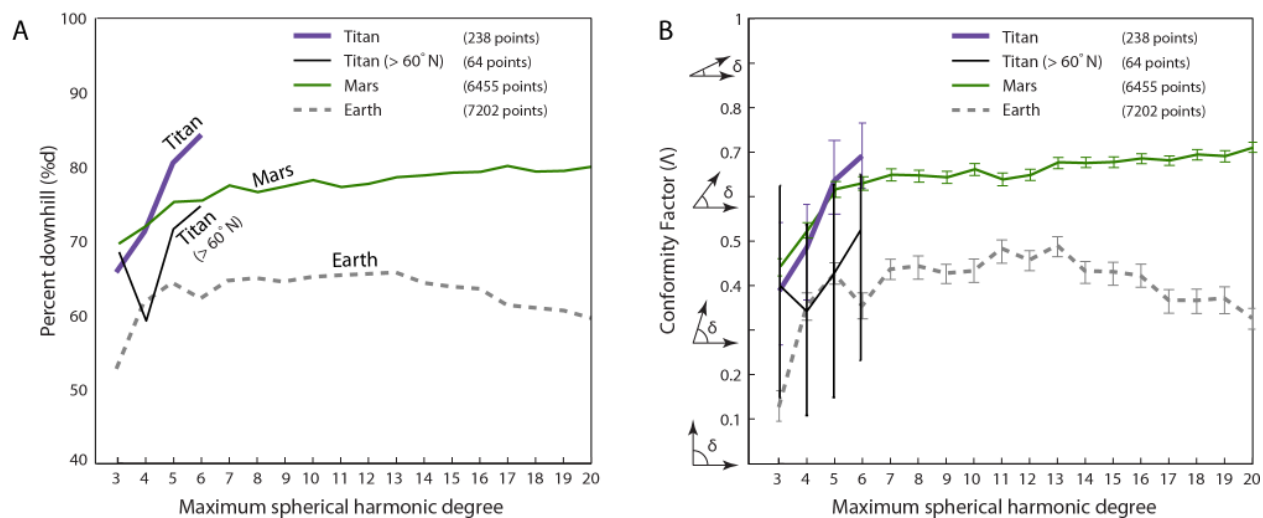


Fig. S3. Long-wavelength topographic conformity is lower in Titan’s north polar region. As in Fig. 2, but including Titan’s north polar region (defined here as the region northwards of 60°N). Error bars in (B) correspond to the 95% confidence interval for the median. The median conformity factor values for Titan’s north polar region at degrees 4-6 are lower than those for Titan as a whole. Given the small sample size, the 95% confidence intervals overlap, but the offset in median values supports differences in the geologic history of Titan’s north polar region relative to the rest of Titan.

582
583

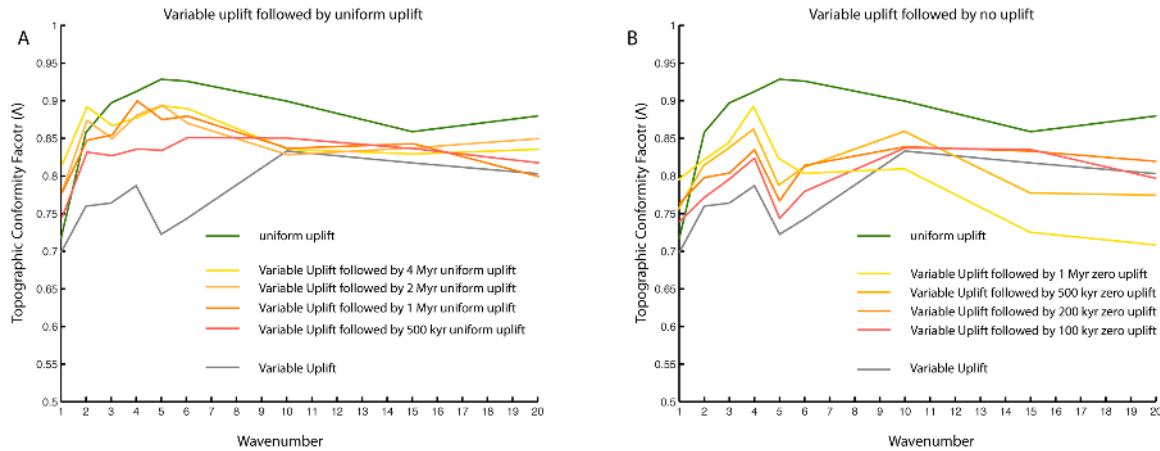
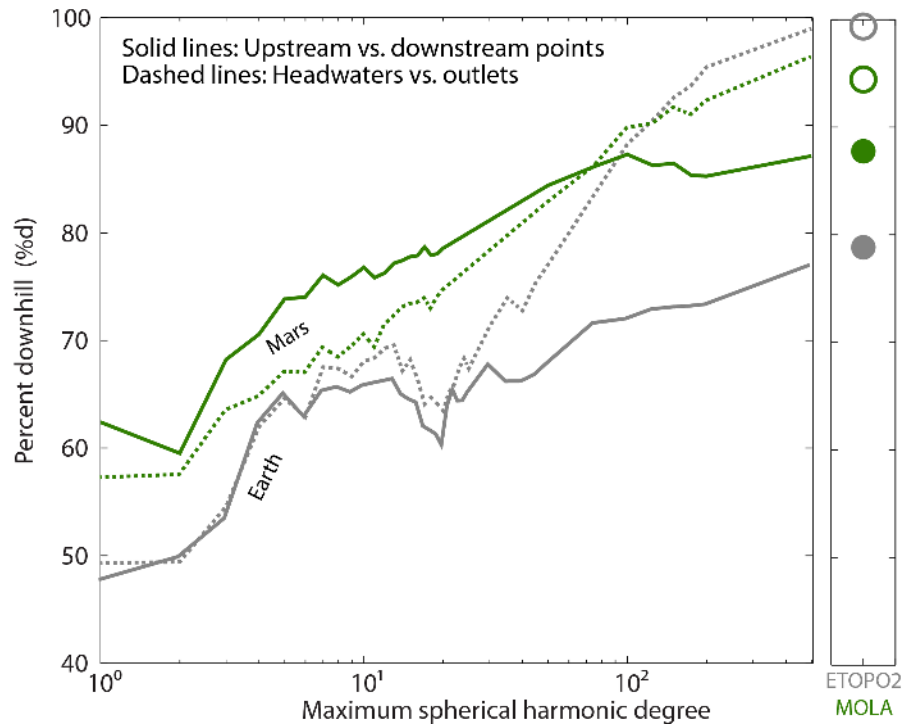


Fig. S4. Drainage networks and deformation interact through time. To investigate how temporal variations in the pattern of deformation influence topographic conformity, we conducted simulations in which variable uplift (which represents dominantly short-wavelength deformation associated with plate tectonics) gave way to either **(A)** uniform uplift, which represents dominantly long-wavelength deformation, or **(B)** zero uplift, which represents tectonic quiescence. Curves represent individual simulations. We find that low \mathcal{A} is a signature of actively generated variable-uplift plate tectonics. If variable uplift is followed by uniform uplift, then the signature of that variable uplift will gradually be erased. If variable uplift is followed by zero uplift, then \mathcal{A} increases at first as drainages conform with topography. Ultimately, landscapes where virtually all relief has been erased can also display poor topographic conformity.



587
588

589 **Fig. S5. Differences in topographic conformity on Mars versus Earth extend to shorter**
 590 **wavelengths.** Solid lines (and filled circles in right panel) show the percent of points that are
 591 uphill (according to the topography at a given spherical harmonic degree) of the nearest
 592 downstream point. Dashed lines (and empty circles in right panel) show the percent of
 593 headwaters that are uphill (according to the topography at a given spherical harmonic degree) of
 594 the drainage network outlet. Small panel at right shows the same metrics computed for the
 595 ETOPO2 gridded 2-minute global relief dataset for Earth (55) and four pixel-per-degree MOLA
 596 topography for Mars (37). We expect %d to reach 100% when topography is perfectly resolved,
 597 drainage networks are perfectly delineated, and drainages have not experienced deformation after
 598 the era of fluvial activity. On Earth, the delineation of fluvial features was performed at 1/8
 599 degree resolution from HydroSHEDS and Hydro1k data (17), distinct from the higher resolution
 600 ETOPO2 dataset, resulting in slight misalignments at the scale at which fluvial valleys are
 601 resolved. These misalignments do not affect long wavelength topographic conformity, because
 602 fluvial valleys are not resolved at these wavelengths. We attribute the plateau in %d on Mars to
 603 deformation after incision of valley networks (24, 25). For Earth and Mars, calculation of %d for
 604 the headwaters versus outlet of each drainage shows that %d values on Earth converge to 100%
 605 across the scale of the drainage, whereas %d values on Mars reach ~95%.

606
607

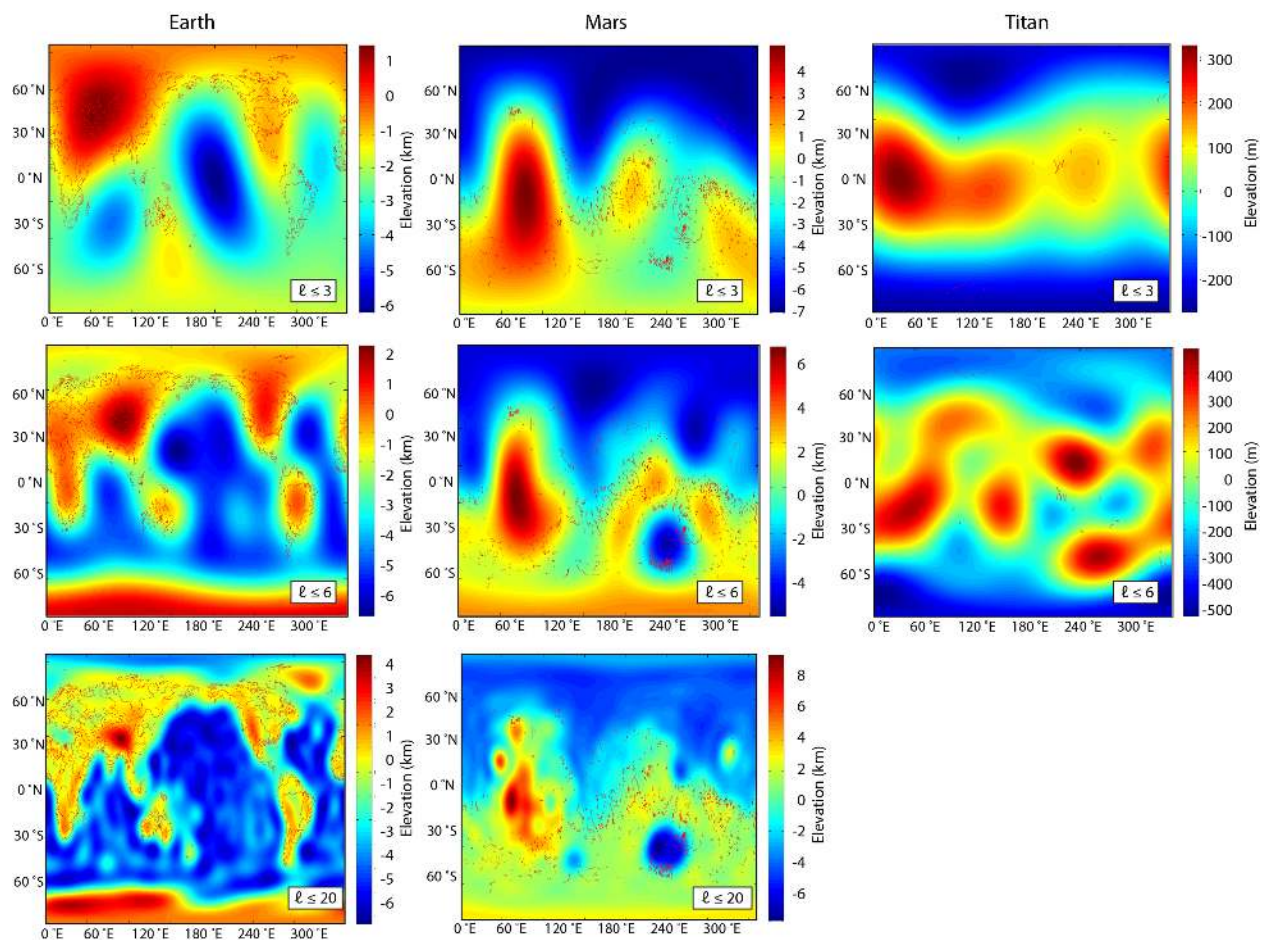


Fig. S6. Spherical harmonic models for the topography of Titan, Earth, and Mars. For Earth and Mars, we show maximum spherical harmonic degrees (ℓ) of 3, 6, and 20. At present, topography is not well constrained for $\ell > 6$ for Titan (21). Coloring reflects elevation referenced to the geoid.

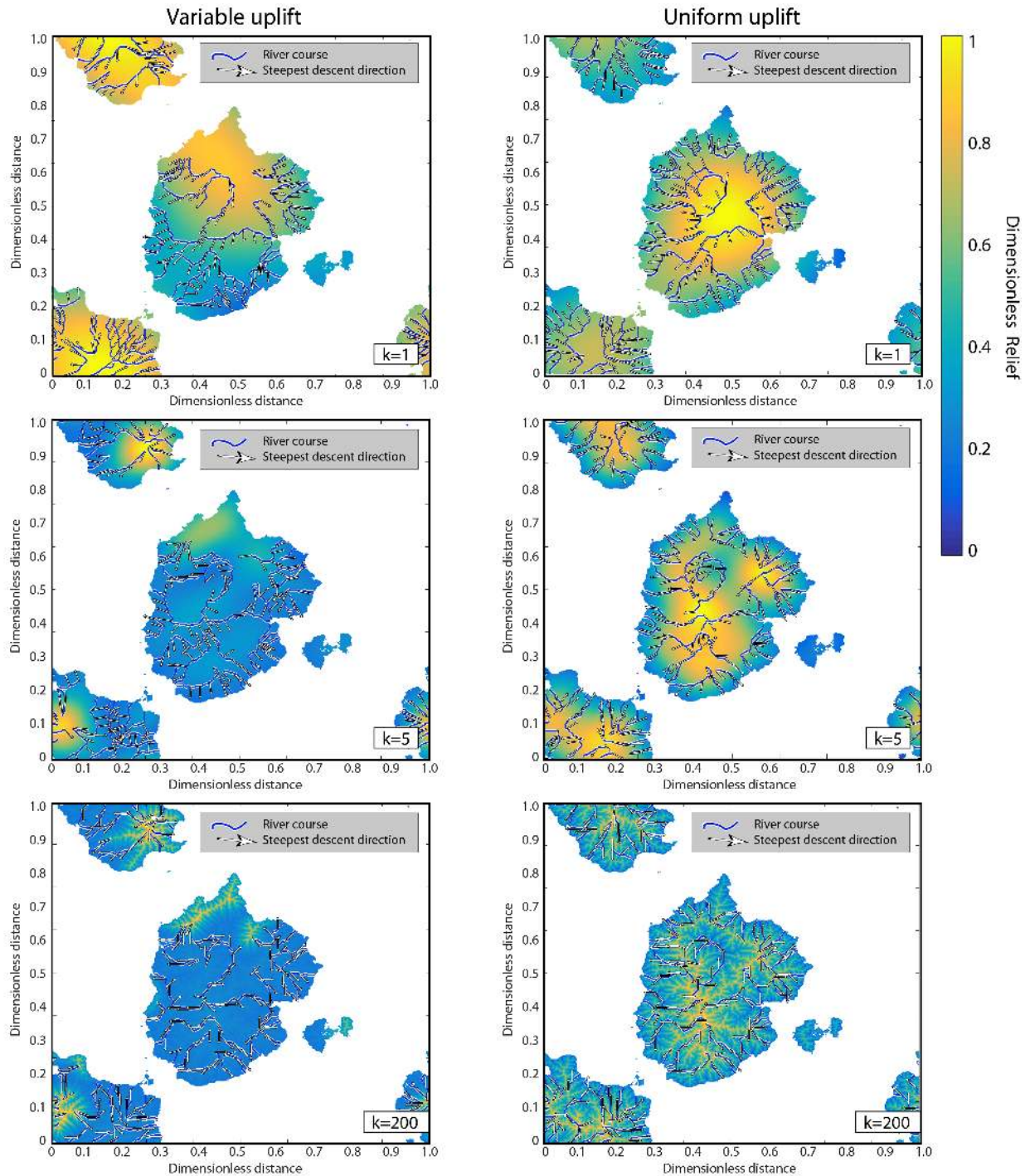


Fig. S7. Example model topography, filtered to increasing maximum spectral wavenumbers. We show the model state at the conclusion of variable uplift (left column) and uniform uplift (right column) runs with identical initial conditions. We filter the topography to maximum spectral wavenumbers of $k=1$, $k=5$, and $k=200$ wavelengths across the domain, as indicated on each panel.

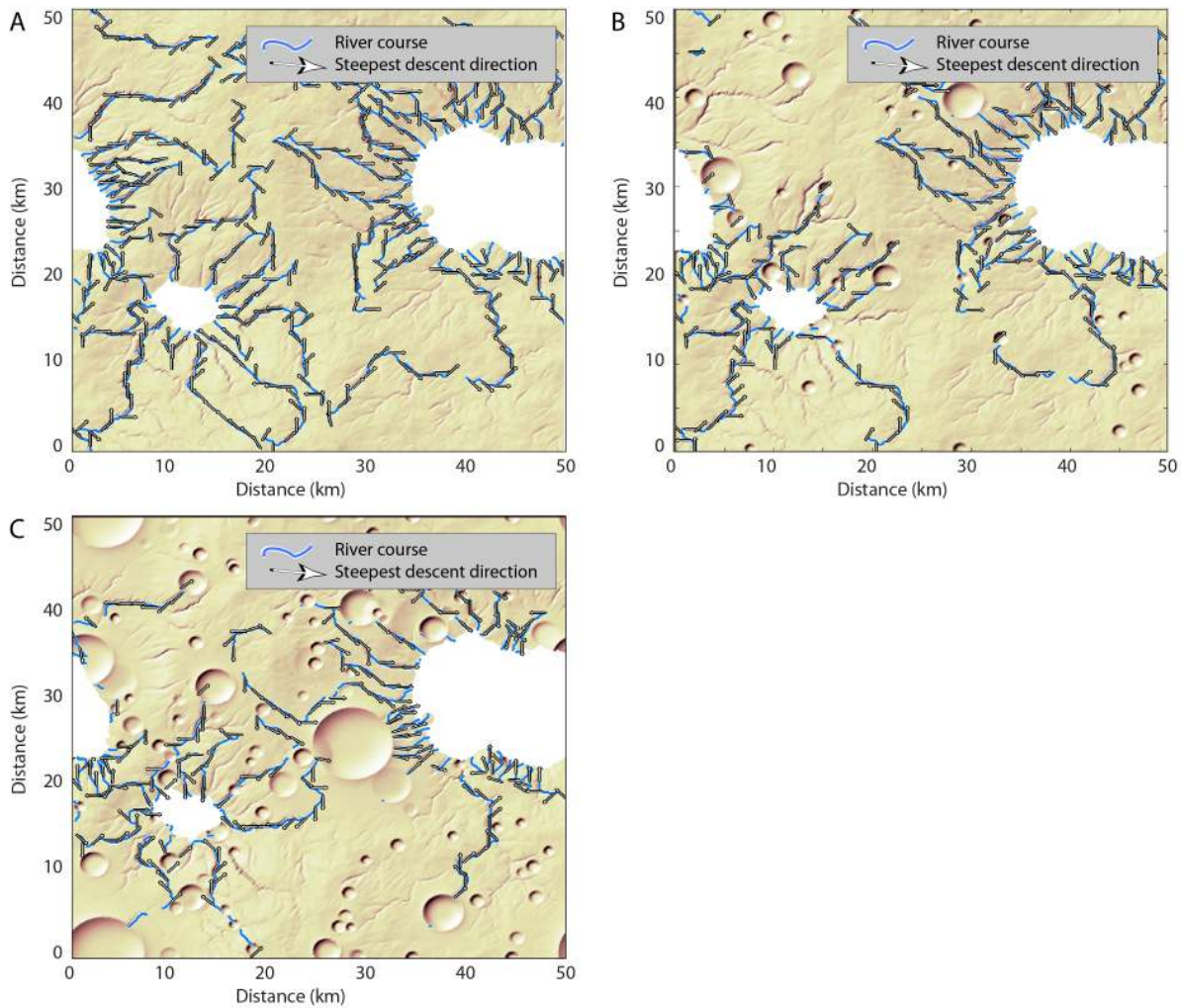


Fig. S8. Shaded relief maps of landscape evolution simulations with cratering. We ran three ensembles (each with ten simulations spanning 60 Myr) to examine the influence of impact cratering on topographic conformity. **(A)** In the control ensemble, fluvial erosion of an initially uncratered surface proceeded without interference. **(B)** We considered fluvial erosion of the same initial surfaces in the control ensemble, but with impact topography superposed on the initial surface as described in the Materials and Methods. **(C)** We also considered fluvial erosion of the same cratered initial surfaces, but with further impacts that occurred during the course of our simulations, disrupting the topography (note the presence of truncated valley networks). This simulation is also shown in Fig. 4A. Each snapshot shows the state of the simulation after 60 Myr.

615
616

617 **Table S1.** Landscape evolution modeling parameters.

Parameter	Value	Notes
Lateral grid dimensions	400 × 400	
Enhanced uplift relative to background uplift	10	Only in variable uplift simulations
Steam power coefficient K	$5 \times 10^6 \text{ m}^{(1.2^m)} \text{ yr}^{-1}$	
Drainage area exponent m	0.5	ref. (40)
Slope exponent n	1.0	ref. (41)
Critical slope	0.6	
Slope of the power spectrum of initial red noise topography	2.0	ref. (27)
Fraction of initial topography assigned to be a fixed base level (to represent oceans)	0.7	
Slope of the power spectrum of red noise surface used to define zones of enhanced uplift in variable uplift simulations	1.3	Only in variable uplift simulations. Less positive values translate to more variance at shorter wavelengths
Fraction of this surface assigned to experience enhanced uplift in variable uplift simulations	0.35	Only in variable uplift simulations.
Simulation duration	10 Myr	

618
619

620 **Table S2.** Landscape evolution modeling parameters for impact cratering simulations.

Parameter	Value	Notes
Lateral grid dimensions	400 × 400	
Lateral grid spacing	125 m × 125 m	
Steam power coefficient K	$1 \times 10^8 \text{ m}^{(1/2^m)} \text{ yr}^{-1}$	
Drainage area exponent m	0.5	ref. (40)
Slope exponent n	1.0	ref. (41)
Critical slope	0.6	
Slope of the power spectrum of initial red noise topography	2.0	ref. (27)
Fraction of initial topography assigned to be a fixed base level (to represent lakes or oceans)	0.1	
Simulation duration	60 Myr	

621

622

623
624
625
626
627
628
629
630

Database S1. Source and sink coordinates for analyzed drainage networks on Titan (see Excel file with tabulated coordinates).